Size Modulation and Heterovalent Doping Facilitated Hybrid Organic and Perovskite Quantum Dot Bulk Heterojunction Solar Cells

Yuhao Li†, Shu Zhou†, Zhiyu Xiong†, Minchao Qin†, Kuan Liu‖, Guilong Cai†, Han Wang‡, Shenghe Zhao‡, Yao-Jane Hsu§, Jianbin Xu‡, and Xinhui Lu†,*

†Department of Physics, The Chinese University of Hong Kong, Shatin 999077, Hong Kong

‡Department of Electronic Engineering, The Chinese University of Hong Kong, Shatin 999077, Hong Kong

§ National Synchrotron Radiation Research Center, Hsinchu 30076, Taiwan

‖ Department of Electronic and Information Engineering, The Hong Kong Polytechnic University, Kowloon 999077, Hong Kong

Corresponding Authors:

*E-mail: xinhui.lu@cuhk.edu.hk

ABSTRACT

Organic photovoltaics and halide perovskite solar cells are both solution processable third-generation photovoltaic devices attracting enormous research attention. In this study, we demonstrate a novel hybrid organic and perovskite PV device by mixing all-inorganic $CsPbI_3$ quantum dots (QDs) into the conventional organic bulk heterojunction active layer of PBDB-T: IT-M. It is found that the charge transfer properties between QDs and organic donor/acceptor (D/A) interfaces can be finetuned with the size modulation and the hetero-valent bismuth (Bi) doping of perovskite QDs, leading to the increase of open circuit voltage. Besides, the incorporation of perovskite QDs with different sizes could effectively modify the nanoscale bulk heterojunction morphology towards more efficient charge collection and thus higher fill factor. The photocurrent of the devices can also be improved through Rayleigh scattering and light absorption of the QDs. As a result, a noticeable enhancement in device performance has been achieved by the PBDB-T: IT-M with 10 nm Bi-doped $CsPbI_3$ QDs device. This work provides one feasible route to fine-tune the energy level alignment and nanophase separation by integrating these two promising PV materials.

1. Introduction

In recent several years, both organic photovoltaics (OPVs) and halide perovskite solar cells (PSCs) have experienced rapid progress in power conversion efficiencies (PCEs). The breakthrough in the synthesis of non-fullerene acceptors has made great contributions to the rapid development of OPVs. Lin et al. synthesized the first high-efficiency non-fullerene small molecule acceptor ITIC in 2015 and the following research based on the ITIC derivatives achieved the record PCE of over 12%.[1-2] Zhang et al. developed a new donor material PBDB-T-2F, further pushing the record PCE over 14%.[3] Recently, the work by Yuan et al. revealed high PCEs over 15% based on a new small molecule acceptor Y6.[4] In the meantime, halide perovskite solar cell has been rising aggressively as it has appropriate bandgap, large absorption coefficient, long exciton diffusion length and high carrier mobility[5-6]. Currently, the certificated PCE record has exceeded 25%, achieved by organic–inorganic hybrid perovskites.[7] And recently, all-inorganic perovskites with potentially better humidity resistance, photostability, and thermal stability, became promising candidates for high-performance photovoltaics.[8-10] Among them, Cubic (α) phase $CsPbI_3$ with a suitable bandgap (E_g=1.73 eV) and wide absorption spectrum, has been widely applied in versatile optoelectronic applications like solar cells, photodetectors[11] and light-emitting diodes[12]. However, the photoactive α phase of $CsPbI_3$ is unstable at room temperature.[13] Instead, fabricating $CsPbI_3$ into quantum dots (QDs) can stabilize the α phase by leveraging the surface energy and reducing the surface defects. To date, $CsPbI_3$-QDs based PSCs have achieved high efficiencies over 14%.[14-16]

Recently, there emerge some interesting studies that wisely combine OPV and PSC materials to stimulate their synergistic strengths, such as broadened absorption, high carrier mobility and efficient charge collection. On one hand, scientists have tried to utilize OPV materials into the PSC device fabrication. For instance, Qin et al. employed a typical fused ring electron acceptor (FREA) ITIC-Th in mixed cation and halide perovskite precursor solution to suppress the formation of yellow (δ) phase and to extend the life time of the precursor solution.[17] Zhang et al. introduced INIC2, another FREA, into the two-step processed $FAMAPb(I,Br,Cl)_3$ perovskite film, which yielded a very impressive PCE of 21.7% with improved stability.[18] Seo group substituted the conventional hole transporting layer spiro-OMeTAD with the donor polymer P3HT and achieved a certified PCE of 22.7% for $(FAPbI_3)_{0.95}(MAPbBr_3)_{0.05}$ system.[19] On the other hand, there's also some research on adding perovskites into OPV devices. $FAPbI_3$ nanocrystals were incorporated into organic solar cells to improve the light harvesting, which successfully increased the short circuit current density (J_{sc}).[20] Guijarro et al. integrated $CsPbI_3$ QDs into the $PTB7$-Th:$PC_{71}BM$ system, which led to an enhancement in exciton separation and the device fill factor (FF).[21] These works have shown a great potential of combining these two powerful PV materials. Further development on mixing strategies and tuning handles is promising to stimulate their synergistic strengths, thus being highly desirable.

Here, we demonstrate a novel hybrid organic and perovskite PV device by mixing all-inorganic $CsPbI_3$ QDs into the conventional organic bulk heterojunction active layer of PBDB-T: IT-M. It is indicated by the photoluminescence (PL) results that there is no

sufficient PL quenching in the 10 nm CsPbI$_3$ QDs and IT-M blend film. We attributed it to the reason that the HOMO of the organic acceptor IT-M (-5.58 eV) and the valence band (VB) of QDs (-5.56 eV) are too close to provide enough driving force for the hole transfer. Remarkably, the charge transfer properties between QDs and organic D/A interfaces can be finetuned by size engineering and heterovalent Bismuth (Bi) doping of perovskite QDs. Doping is one of the common methods to tune the material photophysical and electronic properties[22]. The CsPbI$_3$ QDs with the n-type semiconductor features[23-24] could further achieve n-type doping by the introduction of trivalent ions. The Bi^{3+} is one of the suitable doping materials, which has been widely used to tune the band structure[25-26] and confirmed to stable the phase stability. When the average size of QDs changes from 10 nm to 8 nm, the valence band shift to a higher value of -5.51eV. Similarly, with 0.4 mol% Bi doping, the valence band also upshifts noticeably to -5.50eV. Both ways could enhance the charge transfer between QDs and the acceptor, as evidenced by a higher degree of PL quenching in the blended QDs (8 nm/10 nm Bi-doping):IT-M film. Furthermore, it is found that the incorporation of perovskite QDs with different sizes in organic bulk heterojunction (BHJ) active layer could effectively modify the nanoscale phase separation of organic donor (D) and acceptor (A). The organic intermixing domain sizes (ξ) are largely reduced from 16.5 nm to 12.5 nm, 11.6 nm and 10.6 nm after the incorporation of 8 nm, 10 nm and 10 nm Bi-doped QDs respectively, facilitating the charge collection from the intermixing region. The acceptor domain size (2R$_{g-fractal}$) also decreases slightly, promoting exciton dissociation. In addition, the introduction of CsPbI$_3$ QDs also contributes to the overall

light absorption from their own absorption and increased light scattering within the active layer. Together, the PBDB-T: IT-M with 10 nm Bi-doped QDs device exhibited noticeable improvements in all device characteristics, leading to a 12.2% increase in PCE from the control device without QDs. This work highlights the importance of charge transfer between perovskite QDs and OPV materials when integrating these two PV materials and shows that heterovalent doping and size modification of perovskite QDs can fine-tune the energy alignment and nanophase separation towards better device performance.
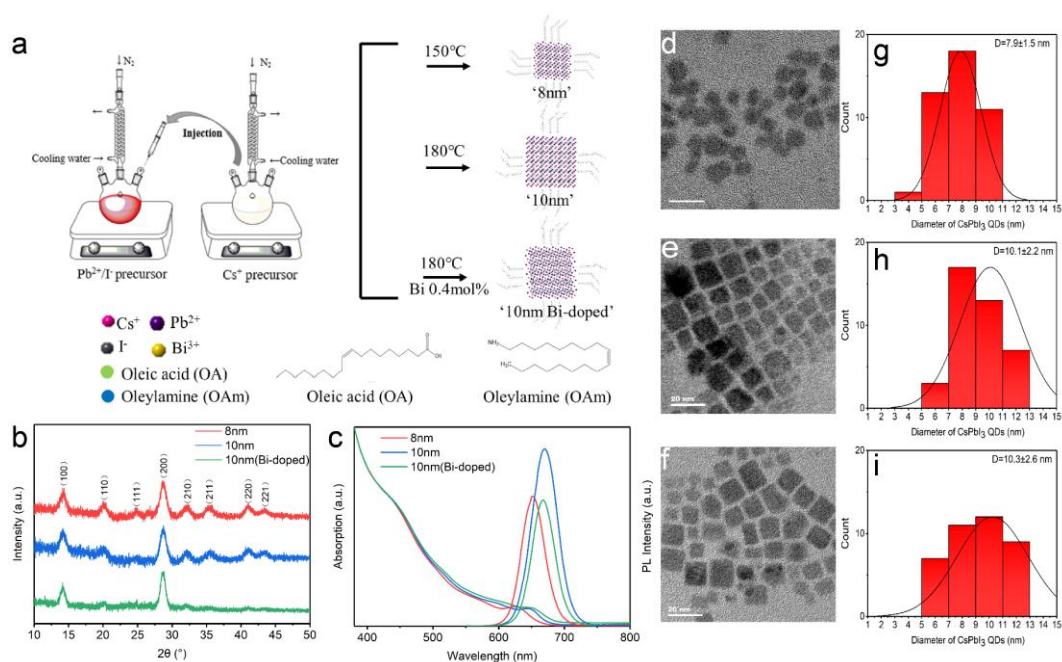
2. Results and Discussion

Figure 1. (a) A schematic view of the $CsPbI_3$ quantum dots (QDs) synthesis process. (b) The XRD patterns of 8 nm, 10 nm, and 10 nm (Bi-doped $CsPbI_3$) QDs films. (c) The corresponding UV/Vis absorption and PL spectra of these three types of $CsPbI_3$ QDs dispersed in hexane. TEM images of (d) 8 nm, (e) 10 nm, and (f) 10 nm (Bi-doped $CsPbI_3$) QDs. (g-i) Size distribution of the three types of $CsPbI_3$ QDs measured from the corresponding TEM images.

$CsPbI_3$ QDs were synthesized via the conventional hot injection method[14-15, 27] by

injecting the Cs_2CO_3 precursor into the pre-heated Pb^{2+}/I^- precursor, as shown in **Figure 1a**. Generally, a higher injection temperature could produce a larger size of $CsPbI_3$ QDs.[14] Thus, we obtained $CsPbI_3$ QDs with two different average sizes at two injection temperatures of 150°C and 180°C. In addition, heterovalent doping of Bi into $CsPbI_3$ QDs were achieved by adding 0.4 mol% BiI_3 into the Pb^{2+}/I^- precursor and hot-injected at 180°C. The higher concentration of bismuth doping (1 mol%) was also achieved, however, the device with the addition of 1 mol% Bi-doped QDs show worse performance at the beginning, may due to the more non-radiative recombination channels by higher Bi doping concertation. Therefore, the 0.4 mol% was considered to be the suitable doping concentration. Successful Bi-doping was confirmed by X-ray photoelectron spectroscopy measurements (**Figure S1a,b**), which clearly present the Bi $4f_{5/2}$ and $4f_{7/2}$ peaks at binding energies of 163.5 eV and 158.3 eV, in consistent with previous reports.[26, 28] **Figure 1d-f** display the TEM images of three types of $CsPbI_3$ QDs synthesized at 150 °C without doping, 180°C without and with Bi doping, respectively. The corresponding size distributions are shown in **Figure 1g-i** by counting over 50 QDs in each group. The average sizes are estimated to be 7.9±1.5 nm, 10.1± 2.2 nm and 10.3±2.6 nm. Therefore, we name them as "8 nm", "10 nm" and "10 nm Bi-doped" $CsPbI_3$ QDs in the following. The shape of 8 nm $CsPbI_3$ QDs is slightly irregular, while the two types of 10 nm QDs exhibit a clear cubic shape.

Figure 1b presents powder X-ray diffraction (XRD) spectra of these three types of $CsPbI_3$ QDs. The (100), (110), (200) diffraction peaks of α-phase[13] can be identified at the diffraction angles (2θ) of 14.2°, 20.1°, 28.7° for all the three types of $CsPbI_3$ QDs,

indicating that both the size change and the bismuth doping don't affect the formation of the desired photoactive α-phase of $CsPbI_3$ QDs. The crystallinity of 10 nm Bi-doped QDs is slightly lower as indicated by the relatively weaker peak intensity, likely arising from defects induced by doping. The optical absorption spectra and photoluminescence (PL) spectra of $CsPbI_3$ QDs in hexane solution are shown in **Figure 1c**. It is seen that the first excitonic peak of these three QDs are located at 646 nm (1.92 eV), 664 nm (1.87 eV) and 665 nm (1.86 eV) for 8 nm, 10 nm and 10 nm Bi-doped $CsPbI_3$ QDs, respectively. Tauc plots of absorption spectra are presented in **Figure S1c**. The corresponding calculated optical band gap are 1.90 eV, 1.85 eV and 1.84 eV, suggesting that bandgap is dominantly controlled by the size of the QDs through the quantum confinement effect.[29-30] It is in accordance with the positions of their PL peaks which are located at 650 nm (1.91 eV), 671 nm (1.85 eV) and 671 nm (1.85 eV). The PL intensity of the 8 nm and 10 nm Bi-doped $CsPbI_3$ QDs are noticeably lower than that of 10 nm $CsPbI_3$ QDs. For the 8 nm QDs, it is attributed to the lower injection temperature and the irregular shape of QDs, while for the 10 nm Bi-doped QDs, it is more likely due to the increase of carrier density as well as defects caused by doping, [28, 31] in agreement with the observed lower crystallinity. Fourier-transform infrared (FTIR) spectroscopy was employed to examine the ligands attached to QDs (**Figure S1d**). After being washed by Methyl acetate (MeOAc) twice, the ligand signals dropped significantly, which improve the conductivity of QDs. Meanwhile, twice-washed QDs remained dispersive in the organic precursor solution without noticeable aggregation.

To investigate the impact of size and doping on the band structure of $CsPbI_3$ QDs,

ultraviolet photoelectron spectroscopy (UPS) measurements were carried out (**Figure S2**). The position of valence band maximum (VBM) with respect to the vacuum level was calculated by subtracting the excitation energy (21.21 eV) with the spectrum width. For undoped $CsPbI_3$ QDs, when the averaged size increases from 8 nm to 10 nm, the VBM shifts downwards from -5.51 eV to -5.56 eV, consistent with previous reports.[23, 32]. Maintaining the size at 10 nm, Bi^{3+} doping induces an upward shifting of VBM back to -5.50 eV. Meanwhile, the $CsPbI_3$ QDs show n-type semiconductor feature according to the UPS data (**Figure S2**), consistent with previous reports[23], the hetero-valent Bi^{3+} doping could further induce n-type doping. **Figure S3a, b** summarizes the PL spectra of pure QD and organic films for comparison. The PL peaks of pure 8 nm, 10 nm $CsPbI_3$,10 nm (Bi-doped) $CsPbI_3$-QDs are located at 660 nm, 676 nm and 674 nm, slightly red-shifted with respect to the solution state values presented in **Figure 1c**, due to the aggregation of QDs in the films.[14] The PL peak of the pure IT-M film is located at 774 nm. The PL response of the pure PBDB-T film is peaked at 690 nm but being much weaker and broadened. There also exists a shoulder at ~750 nm for pure PBDB-T film, which is associated with the strong π-π interaction between conjugated groups of PBDB-T[33]. Combining the VBM and the estimated conduction band minimum (CBM) (CBM = VBM + optical energy gap (E_{opt})) of the $CsPbI_3$ QDs and previously reported HOMO/LUMO levels of PBDB-T and IT-M[34], we plot the energy level alignment of $CsPbI_3$ QDs and OPV materials in **Figure 2a**. Note here E_{opt} is estimated from the first excitonic peak of the QD solution, considering that the incorporation concentration of QDs is very low and well dispersed in the organic BHJ active layer
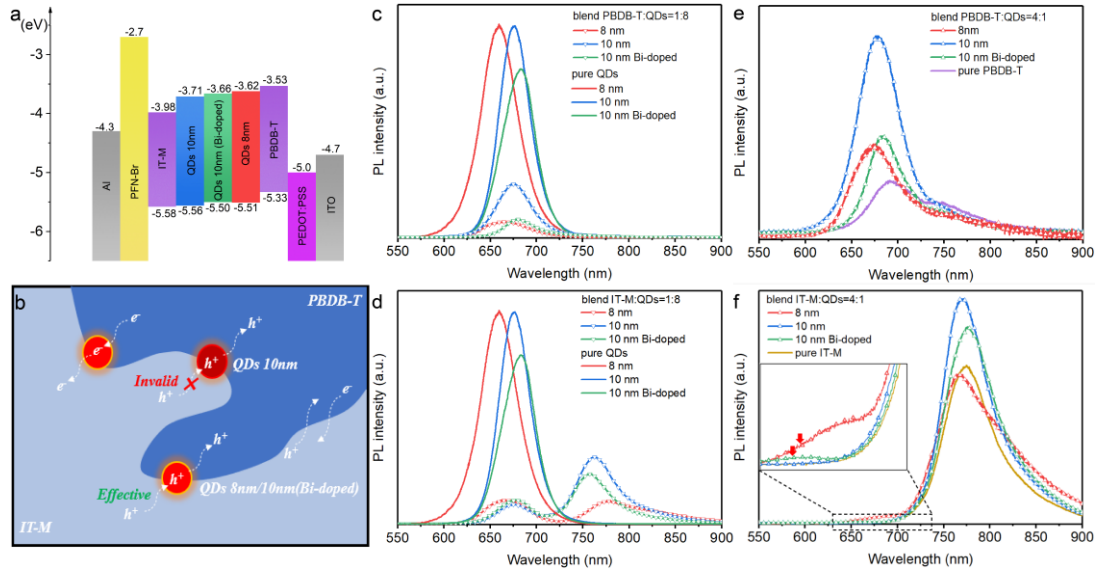
Figure 2. (a) Energy alignment of CsPbI$_3$ QDs and OPV materials. (b) Schematic of the charge transfer between the CsPbI$_3$ QDs and PBDB-T, IT-M. PL spectra of binary PBDB-T: CsPbI$_3$ QDs film (c) and binary IT-M: CsPbI$_3$ QDs film (d) with mass ratio=1:8. PL spectra of binary PBDB-T: CsPbI$_3$ QDs film (e) and binary IT-M: CsPbI$_3$ QDs film (f) with mass ratio=4:1.

without aggregation.

PL measurements for blend films are further measured to understand the charge transfer properties between CsPbI$_3$ QDs and OPV materials. The charge transfer is influenced by many factors (energy offset, transfer integral, reorganization energy, etc.), however for the three types of QDs in comparison, we employ the same ligands and ligand treatments, which indicates the interface condition between OPV materials and QDs are considered unchanged. Consequently, we believe the energy offset induced by size modulation and heterovalent doping should be the most possible reason affecting the charge transfer and thereby device performance improvement here. We firstly show the PL spectra of ternary PBDB-T: IT-M: CsPbI$_3$ QDs (addition: 0.30 wt.%) films (**Figure S3c**). Generally, the quenching of PBDB-T: IT-M blend is stronger with the

incorporation of all the three types of CsPbI$_3$ QDs (**inset of Figure S3c**). However, the quenching for the film with 10 nm CsPbI$_3$ QDs is less effective than the other two films. To figure out the reasons, we perform the PL measurement of the binary organics/QDs film in the following. Due to the partial overlapping of absorption spectra of PBDB-T, IT-M and QDs, it is difficult to selectively excite desired components. Therefore, we made binary films with extreme mass ratios and investigate the PL quenching behaviors to understand the charge transfer from the dominant component to the minor component. First, the PL spectra of blend PBDB-T: QD (1:8) and IT-M: QD (1:8) films are presented in **Figure 2c and d** to examine the charge transfer behavior from QD to organic phases. Compared with pure QD films, the PL intensities of these blend films with the same population of QDs all quench significantly. It demonstrates that the exciton generated in all three types of QDs can be successfully dissociated at PBDB-T/QD and IT-M/QD interfaces through hole transfer and electron transfer respectively. This is also consistent with QD's relatively larger HOMO offset with PBDB-T and LUMO offset with IT-M. Interestingly, the PL quenching for 8nm QDs is stronger compared to that of 10 nm QDs although the LUMO energy offset between 10 nm QDs and PBDB-T is even larger. This is possible due to the same mass ratio of PBDB-T and all types of QDs, the 8 nm QDs with relatively smaller volume could form more QDs/organics interfaces, leading to more obvious PL quenching. Then, we discuss the charge transfer behavior from organic phases to QDs based on the PL spectra of binary PBDB-T: QDs (4:1) and IT-M: QDs (4:1) films. For the PBDB-T: QDs (4:1) film (**Figure 2e**), the PL signal around ~750 nm originated from PBDB-T shows certain degree of quenching, but not

as much as the quenching of QDs. We further fit the PL intensity profiles of PBDB-T: QDs with a Gaussian for QDs and the PL profile of pure PBDB-T to estimate the quenching degree of PBDB-T, as illustrated in **Figure S4**. The PL intensity originated from PBDB-T shows ~ 30% of quenching when blended with all three kinds of QDs, demonstrating the existence of electron transfer from PBDB-T to the QDs. In contrast, IT-M: QDs (4:1) films show no quenching or even higher of IT-M PL signal (**Figure 2f**), indicating that the charge transfer is still dominant electron transfer from QDs to IT-M, while the hole transfer from IT-M to QDs is not as obvious due to insufficient HOMO offsets. Note here, the PL signals in the QD region (at ~680 nm) are different as shown in the insert of **Figure 2f**. For the IT-M/8 nm and 10 nm Bi-doped QDs (4:1) film, we can observe PL increase of QDs, suggesting that the hole transfer channels from IT-M are still effective for these two types of QDs. In conclusion, for binary IT-M/QDs film, the excitons excitation happens in both IT-M and QD regions. The charge transfer between the QDs and IT-M consist of the electron transfer from QDs to IT-M and the hole transfer from IT-M to QDs. The PL spectra of IT-M: QDs (1:8) films (**Figure 2d**) reveal that, when the amount of QDs is dominant, the electron transfer from QDs to IT-M is strong and sufficient. This explain the increase of PL intensity when the amount of IT-M becomes dominant in the IT-M:QDs (4:1) films, most of the radiative recombination happen inside the IT-M because of the efficient electron transfer from the QDs. However, for 8 nm and 10 nm Bi-doped QDs, there's still hole transfer channels from the IT-M to QDs, giving rise to some radiative recombination in QDs as manifested in the insert of **Figure 2f**. In summary, **Figure 2b** illustrates the

charge transfer pathways between PBDB-T, IT-M and QDs. For the 8nm and 10 nm Bi-doped $CsPbI_3$ QDs, the bidirectional electron/hole transfer are both effective. Particularly for the 10 nm $CsPbI_3$ QDs, the hole transfer from IT-M to QDs is hindered.

To examine the influence of incorporating $CsPbI_3$ QDs on the morphology of the PBDB-T:IT-M active layer, grazing incidence small-angle/wide-angle X-ray scattering (GISAXS/GIWAXS) measurements were performed to probe nanoscale and molecular level morphology. **Figure 3a-d** presents the two-dimensional (2D) GISAXS patterns, while **Figure 3e** shows the corresponding GISAXS intensity profiles along the in-plane direction. The intensity profiles are fitted with the Debye–Anderson–Brumberger (DAB) model and the fractal-like network model to quantify the correlation length (ξ) of intermixing amorphous phase and the average domain size ($2R_g$) of IT-M phases.[35-37] Here the intermixing domain means the amorphous region with mixed donor and acceptor. Since both donor and acceptor are semi-crystalline, it is well accepted to model the constitution of active layer into three kinds: pure donor crystalline domain, pure acceptor crystalline domain and intermixing donor and acceptor amorphous region[38-40]. Due to the contrast in electron density, we can use GISAXS to probe the averaged domain sizes. In the D/A intermixing region, there is abundant D/A interfaces, so exciton dissociation is sufficient. However, the dissociated electrons and holes will largely recombine due to the lack of connected charge transport pathways. Therefore, a smaller intermixing region will help the dissociated charges transport to pure domains to reach the corresponding electrode, thus facilitate the charge collection from the intermixing region. The fitted parameters are summarized in **Table S1**. It is evident that

the addition of all the three types of CsPbI$_3$ QDs could largely shrink the amorphous intermixing domain, the organic intermixing domain sizes (ξ) are reduced from 16.5 nm to 12.5 nm, 11.6 nm and 10.6 nm after the addition of 8 nm, 10 nm and 10 nm Bi-doped QDs respectively, as the QDs are mainly dispersed in the amorphous region. This could promote the exciton utilization from amorphous regions. The size of pure IT-M domains remains almost unchanged before and after adding QDs, implying that QDs does not affect the aggregation of acceptor crystalline domains. It is further supported by GIWAXS measurements (**Figure 3f and S5**) that the GIWAXS profiles of the PBDB-T:IT-M blend film without and with QDs indicate a preferential face-on oriented molecular packing: the π-π stacking peaks appear in the out-of-plane direction at q_z = 1.75 Å^{-1} (d = 3.59 Å) and the lamellar scattering peaks are located at q_r = 0.272 Å^{-1} (d
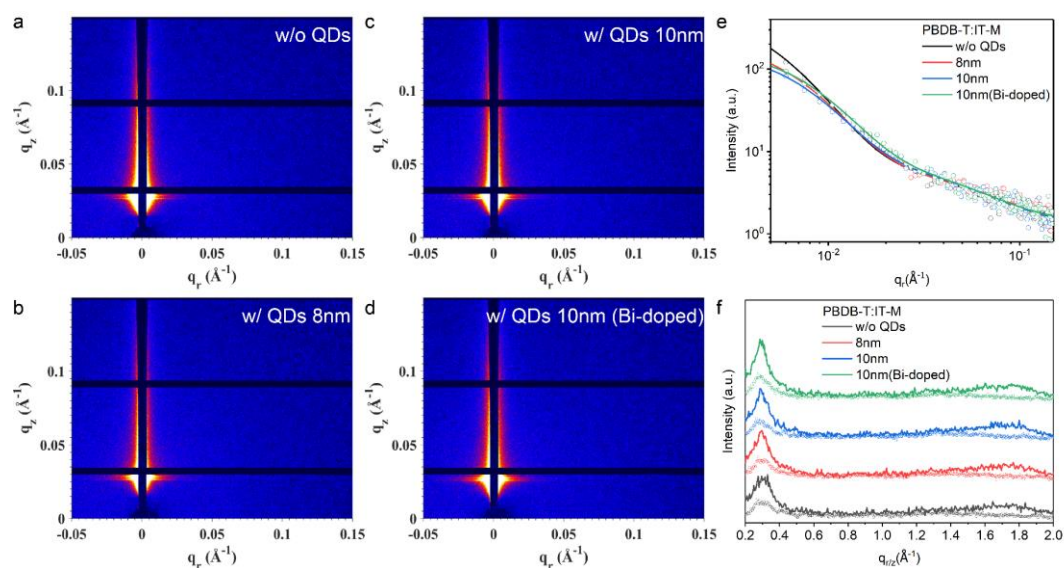

Figure 3. 2D GISAXS patterns of PBDB-T: IT-M films (a)w/o QDs, (b) w/ QDs 8 nm, (c) w/ QDs 10 nm, (d) w/ QDs 10 nm Bi-doped (the addition amount: 0.30wt.%). (e) The corresponding GISAXS intensity profiles (dotted lines) and best fittings along the in-plane direction (solid lines). (f) GIWAXS intensity profiles along the in-plane (dotted lines) and out-of-plane (solid lines) directions.

= 23.1 Å). The charge collection and transfer properties of the films are further characterized by time-resolved photoluminescence (TRPL) measurement excited at 636 nm (**Fig. S6**) and the corresponding data are summarized in **Table S2**. The average carrier lifetime of PBDB-T: IT-M without and with 0.3 wt.% of 8 nm, 10 nm and 10 nm Bi-doped QDs are 3.86 ns, 3.46 ns, 3.57 ns and 3.52 ns, respectively. We attribute the similar lifetime to the same host materials, PBDB-T: IT-M. Nevertheless, the carrier lifetime is in overall shortened with QDs, suggesting the more efficient charge transfer and charge collection between the donor (D) and acceptor (A), which is well matched with observed shrunken intermixing phase (shown in **Table S1**). The relatively smaller intermixing phase will increase the D/A interfaces, facilitate the charge transfer and collection efficiency.

To understand the influence of adding QDs to the device performance, solar cells were fabricated with the conventional OPV device structure ITO/PEDOT:PSS/Active layer/PFN-Br/Ag, as shown in **Figure 4a**.[34, 38] UV/Vis absorption spectra of PBDB-T:IT-M films without and with 0.3 wt.% QDs are presented in **Figure 4b**. In compared with the film without QDs, the light absorption of the films with QDs show enhancement throughout the whole absorption spectrum. It is usually attributed to the Rayleigh scattering induced by adding QDs[23, 38]. The larger the QDs are, the stronger the Rayleigh scattering will be induced. Besides, there's some extra light absorption enhancement in the 350 nm-400 nm region, which could be contributed to the light absorption of $CsPbI_3$ QDs.[42-43] **Figure 4c** shows current density versus voltage ($J–V$) curves of the OPV devices without and with $CsPbI_3$ QDs. The photovoltaic parameters
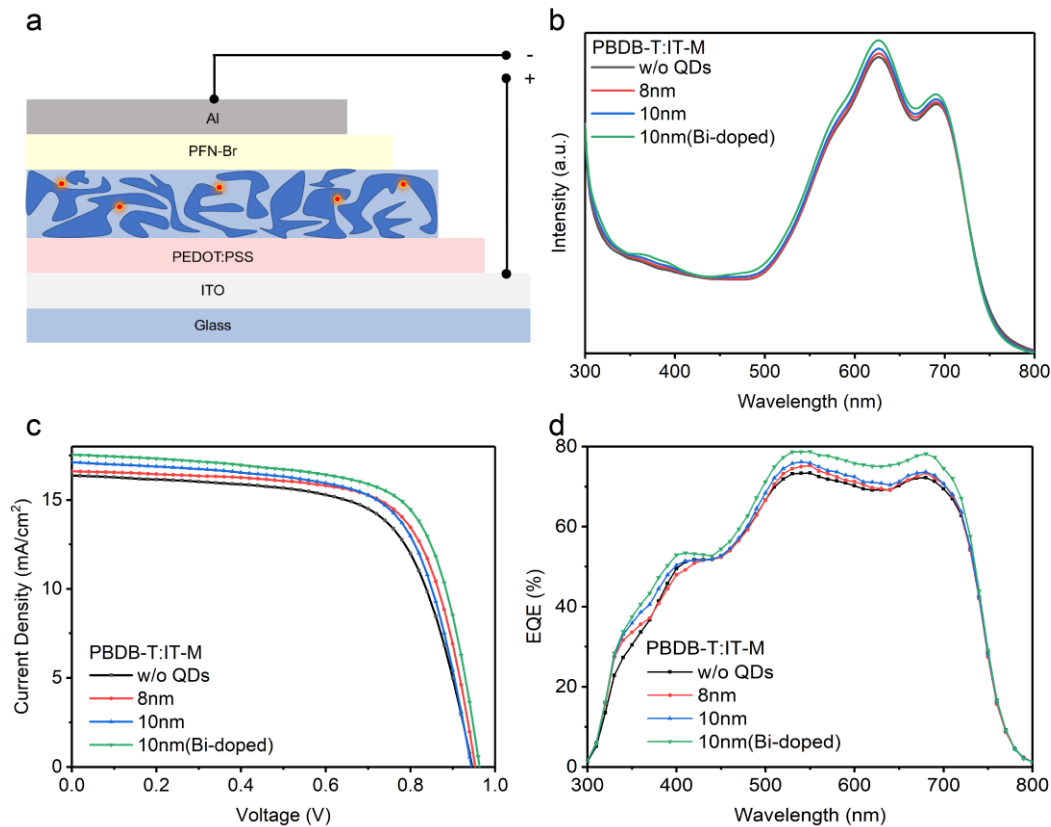
Figure 4. (a) Device architecture of PBDB-T:IT-M with CsPbI$_3$ QDs. (b)UV/Vis absorption spectra of PBDB-T:IT-M films without and with 0.3 wt.% 8 nm, 10 nm, 10 nm (Bi-doped) CsPbI$_3$ QDs. (c) Current density–voltage (J–V) curves and (d) EQE of the best devices.

of the devices are summarized in **Table 1**. To be noticed, the device performance of organic solar cells is highly dependent on the organic materials quality. The properties (bandgaps, LUMO/HOMO, etc.) of the organic materials change with the material batches, especially the polymer donor PBDB-T is highly related with the molecular weight. Therefore, the device performance will show large variation when the organic material batches are different, this is further convinced by the optimized thermal annealing temperature for PBDB-T: IT-M thin films, which is 80℃ rather than 160 ℃ by previous papers[34]. All the devices with QDs show relatively larger J_{sc} than the control device without QDs. The corresponding external quantum efficiency (EQE)

spectra are plotted in **Figure 4d**. The small deviation of the calculated J_{sc} from the measured J_{sc} further confirms the enhancement in photocurrent. We attribute the J_{sc} enhancement to both the gain from light absorption and the improved exciton utilization from the intermixing region after the addition of QDs. We can also observe an overall improvement in fill factor (FF) after the incorporation of QDs. To understand the change of FF, the space charge limited current (SCLC) method was adopted to compare the charge transport properties of the PBDB-T: IT-M without and with $CsPbI_3$ QDs (**Figure. S7**). The hole-only devices were fabricated using the structure of ITO/PEDOT: PSS/ Active layer /MoO_x/Au, while the electron-only devices were fabricated using the structure of ITO/ ZnO/Active layer/PFN-Br/Al. The hole mobilities of PBDB-T: IT-M without and with 0.3 wt.% addition of 8 nm, 10 nm and 10 nm Bi-doped QDs were measured to be 3.68×10^{-4}, 5.05×10^{-4}, 3.88×10^{-4} and 5.19×10^{-4} $cm^2V^{-1}s^{-1}$. And for the electron mobilities, the values are 2.24×10^{-5}, 3.97×10^{-5}, 2.91×10^{-5} and 3.51×10^{-5} $cm^2V^{-1}s^{-1}$ respectively. The slightly increased carrier mobility may due to the decreased amorphous intermixing phase (**Table S1**), which is of benefit for the pure donors and acceptors to form more charge transport channels. The improved carrier mobility well accords with the enhanced device fill factor (FF) shown in **Table 1**.

Interestingly, an obvious increase in open circuit voltage (V_{oc}) was obtained in the devices with 8 nm and 10 nm Bi-doped $CsPbI_3$ QDs, while device with 10 nm QDs does not show such improvement. This is correlated with the more efficient hole transfer from IT-M to 8 nm and 10 nm Bi-doped $CsPbI_3$ QDs due to the size and doping induced larger HOMO offset with IT-M. It is therefore suggested that a fine control over energy

level alignment between QDs and OPV materials can effectively reduce the V_{oc} loss. Light-dependent J-V measurements were measured to investigate V_{oc} loss and charge-recombination mechanism. The J_{SC} versus light intensity curve was fitted with the formula of $J_{SC} \propto P_{light}^{\alpha}$ (**Figure R2a)**. The exponent α for the devices based on the PBDB-T:IT-M w/o and w/ 8nm, 10nm, 10nm Bi-doped QDs were 0.982, 0.999, 0.983 and 0.993, respectively. The higher exponents closer to 1 for films with 8 nm and 10 nm Bi-doped QDs suggest that less bimolecular recombination was obtained in compared with that of the pure organic bulk heterojunction, in consistent with observed device performance. Then, the V_{OC} versus P_{light} curves were plotted and fitted with the formula of $V_{OC} \approx n k_B T/q \ln(P_{light})$. where k_B is the Boltzmann constant, T is temperature and q is elementary charge. The ideality factors n of PBDB-T:IT-M w/o and w/ 8nm, 10nm, 10nm Bi-doped QDs-based devices are calculated to be 1.365, 1.183, 1.090 and 1.102 $k_B T/q$ (T=300K) respectively (**Figure R2b)**. The results suggest that the trap-assisted recombination here is rather minor and bimolecular recombination should be the dominate mechanism at open circuit conditions, which is common for organic solar cells. Overall, the n value was decreased after adding of QDs into the PBDB-T: IT-M system, which could be attributed to the reduction of amorphous intermixing phase as shown in **Table S1.** Owning to the strongest light absorption, cascaded energy alignment and suppressed recombination, the device based on 10 nm Bi-doped QDs exhibited the best PCE of 11.64%, a 12.2% increase in PCE compared with the control device.

Table 1. The photovoltaic performance of the devices based on PBDB-T:IT-M with the addition of 0.30 wt.% $CsPbI_3$ QDs of different types (D=8 nm, 10 nm, 10 nm Bi-doped).

		V_{oc} (V)	J_{sc} (mA cm^{-2})	FF (%)	PCE (%)	Relative PCE enhancement (%)	Calculated J_{sc} (mA cm^{-2})
Control	Average	0.945	16.40	66.9	10.37±0.22	—	
	Best	0.947	16.49	68.2	10.65	—	15.51
8 nm	Average	0.952	16.45	68.4	10.72±0.17	3.3±1.6	
	Best	0.953	16.61	69.5	11.01	6.2	15.61
10 nm	Average	0.946	16.84	68.2	10.87±0.05	4.8±0.4	
	Best	0.948	16.73	69.0	10.94	5.5	15.86
10 nm Bi-doped	Average	0.964	16.95	69.2	11.29±0.23	8.1±2.3	
	Best	0.963	17.55	68.9	11.64	12.2	16.62

The device performance of adding different concentration (0.15, 0.30 and 0.60 wt.%) of $CsPbI_3$ QDs was also investigated (**Figure S9**). Detailed photovoltaic parameters were listed in **Table S3-5**. It is found that FF and V_{oc} increases generally when increasing the concentration of incorporated QDs. However, when the concentration is higher than 0.30 wt.%, J_{sc} starts to decrease, possibly due to the enhanced recombination caused by the aggregation of higher concentration of $CsPbI_3$ QDs.[21] The surface morphology of the films was further examined by AFM and SEM measurements. **Figure S10** show the AFM images of the top surface of PBDB-T:IT-M films without and with 10 nm (Bi-doped) $CsPbI_3$ QDs (0.30 wt.%). The surface roughness didn't change significantly, being 2.8 nm with $CsPbI_3$ QDs and 3.0 nm without $CsPbI_3$ QDs. The slightly smoother top surface with $CsPbI_3$ QDs might contribute to smaller interfacial recombination. The corresponding SEM images are shown in **Figure S11**, which also shows no obvious difference. We attribute the almost the same surface morphology to the small amount (0.15 wt.%-0.60 wt.%) of QDs added

in the hybrid devices, which have little influence on the surface change. Besides, it also suggests that QDs are well embedded in the active layer instead of aggregated at the surface.

Conclusion

In summary, we fabricate a novel hybrid organic and perovskite PV device by mixing $CsPbI_3$ QDs into a conventional organic system PBDB-T: IT-M. The energy level alignment of QDs and OPV materials was effectively tuned by changing the QDs size and heterovalent doping to facilitate charge transfer between perovskite QDs and OPV materials. The BHJ film morphology, particularly the size of the intermixing amorphous region was also modified for more efficient exciton collection. All these contribute to a considerable decrease of charge recombination and in turn an increase of FF, V_{oc} and J_{sc}. Furthermore, the incorporation of $CsPbI_3$ QDs also improves the photocurrent of the devices through Rayleigh scattering and their own light absorption. Consequently, a maximum increase of 12.2% in PCE has been achieved, compared with control device. This work suggests one feasible route to integrate these two promising PV materials, which potentially combines their mutual strength.

Supporting Information

Supporting Information is available from the Wiley Online Library or from the author.

References

(1) Lin, Y. Z.; Wang, J. Y.; Zhang, Z. G.; Bai, H. T.; Li, Y. F.; Zhu, D. B.; Zhan, X. W., An Electron Acceptor Challenging Fullerenes for Efficient Polymer Solar Cells. *Adv. Mater.* **2015,** *27*, 1170-1174.

(2) Zhao, F. W.; Dai, S. X.; Wu, Y. Q.; Zhang, Q. Q.; Wang, J. Y.; Jiang, L.; Ling, Q. D.; Wei, Z. X.; Ma, W.; You, W.; Wang, C. R.; Zhan, X. W., Single-Junction Binary-Blend Nonfullerene Polymer Solar Cells with 12.1% Efficiency. *Adv. Mater.* **2017,** *29*, 1700144.

(3) Zhang, H.; Yao, H. F.; Hou, J. X.; Zhu, J.; Zhang, J. Q.; Li, W. N.; Yu, R. N.; Gao, B. W.; Zhang, S. Q.; Hou, J. H., Over 14% Efficiency in Organic Solar Cells Enabled by Chlorinated Nonfullerene Small-Molecule Acceptors. *Adv. Mater.* **2018,** *30*, 1800613.

(4) Yuan, J.; Zhang, Y. Q.; Zhou, L. Y.; Zhang, G. C.; Yip, H. L.; Lau, T. K.; Lu, X. H.; Zhu, C.; Peng, H. J.; Johnson, P. A.; Leclerc, M.; Cao, Y.; Ulanski, J.; Li, Y. F.; Zou, Y. P., Single-Junction Organic Solar Cell with over 15% Efficiency Using Fused-

Ring Acceptor with Electron-Deficient Core. *Joule* **2019,** *3*, 1140-1151.

(5) Im, J. H.; Lee, C. R.; Lee, J. W.; Park, S. W.; Park, N. G., 6.5% Efficient Perovskite Quantum-Dot-Sensitized Solar Cell. *Nanoscale* **2011,** *3*, 4088-4093.

(6) Correa-Baena, J. P.; Abate, A.; Saliba, M.; Tress, W.; Jacobsson, T. J.; Gratzel, M.; Hagfeldt, A., The Rapid Evolution Of Highly Efficient Perovskite Solar Cells. *Energy Environ. Sci.* **2017,** *10*, 710-727.

(7) *NREL. Research Cell Efficiency Record. 2019.* **Accessed Feb 2020.,** *https://www.nrel.gov/pv/assets/pdfs/best-research-cell-efficiencies.20200218.pdf.*

(8) Zhang, J. R.; Hodes, G.; Jin, Z. W.; Liu, S. Z., All-Inorganic $CsPbX_3$ Perovskite Solar Cells: Progress and Prospects. *Angew. Chem. Int. Ed.* **2019,** *58*, 15596-15618.

(9) Wang, Y.; Dar, M. I.; Ono, L. K.; Zhang, T. Y.; Kan, M.; Li, Y. W.; Zhang, L. J.; Wang, X. T.; Yang, Y. G.; Gao, X. Y.; Qi, Y. B.; Gratzel, M.; Zhao, Y. X., Thermodynamically Stabilized Beta-$CsPbI_3$-based Perovskite Solar Cells With Efficiencies > 18%. *Science* **2019,** *365* , 591-595.

(10) Nenon, D. P.; Christians, J. A.; Wheeler, L. M.; Blackburn, J. L.; Sanehira, E. M.; Dou, B. J.; Olsen, M. L.; Zhu, K.; Berrya, J. J.; Luther, J. M., Structural And Chemical Evolution of Methylammonium Lead Halide Perovskites during Thermal Processing From Solution. *Energy Environ. Sci.* **2016,** *9*, 2072-2082.

(11) Zheng, J. T.; Luo, C. Z.; Shabbir, B.; Wang, C. J.; Mao, W. X.; Zhang, Y. P.; Huang, Y. M.; Dong, Y. M.; Jasleniak, J. J.; Pan, C. X.; Bao, Q. L., Flexible Photodetectors based on Reticulated SWNT/Perovskite Quantum Dot Heterostructures with Ultrahigh Durability. *Nanoscale* **2019,** *11*, 8020-8026.

(12) Chiba, T.; Hayashi, Y.; Ebe, H.; Hoshi, K.; Sato, J.; Sato, S.; Pu, Y. J.; Ohisa, S.; Kido, J., Anion-Exchange Red Perovskite Quantum Dots with Ammonium Iodine Salts for Highly Efficient Light-Emitting Devices. *Nature Photon.* **2018,** *12*, 681-687.

(13) Eperon, G. E.; Paterno, G. M.; Sutton, R. J.; Zampetti, A.; Haghighirad, A. A.; Cacialli, F.; Snaith, H. J., Inorganic Caesium Lead Iodide Perovskite Solar Cells. *J. Mater. Chem. A* **2015,** *3*, 19688-19695.

(14) Swarnkar, A.; Marshall, A. R.; Sanehira, E. M.; Chernomordik, B. D.; Moore, D. T.; Christians, J. A.; Chakrabarti, T.; Luther, J. M., Quantum Dot-induced Phase Stabilization of Alpha-CsPbI$_3$ Perovskite for High-Efficiency Photovoltaics. *Science* **2016,** *354*, 92-95.

(15) Sanehira, E. M.; Marshall, A. R.; Christians, J. A.; Harvey, S. P.; Ciesielski, P. N.; Wheeler, L. M.; Schulz, P.; Lin, L. Y.; Beard, M. C.; Luther, J. M., Enhanced Mobility CsPbI$_3$ Quantum Dot Arrays for Record-Efficiency, High-Voltage Photovoltaic Cells. *Sci. Adv.* **2017,** *3*, eaao4204.

(16) Chen, K. Q.; Jin, W.; Zhang, Y. P.; Yang, T. Q.; Reiss, P.; Zhong, Q. H.; Bach, U.; Li, Q. T.; Wang, Y. W.; Zhang, H.; Bao, Q. L.; Liu, Y. L., High Efficiency Mesoscopic Solar Cells Using CsPbI$_3$ Perovskite Quantum Dots Enabled by Chemical Interface Engineering. *J. Am. Chem. Soc* **2020,** *142*, 3775-3783.

(17) Qin, M. C.; Cao, J.; Zhang, T. K.; Mai, J. Q.; Lau, T. K.; Zhou, S.; Zhou, Y.; Wang, J. Y.; Hsu, Y. J.; Zhao, N.; Xu, J. B.; Zhan, X. W.; Lu, X. H., Fused-Ring Electron Acceptor ITIC-Th: A Novel Stabilizer for Halide Perovskite Precursor Solution. *Advanced Energy Materials* **2018,** *8*, 1703399.

(18) Zhang, M. Y.; Dai, S. X.; Chandrabose, S.; Chen, K.; Liu, K.; Qin, M. C.; Lu, X. H.; Hodgkiss, J. M.; Zhou, H. P.; Zhan, X. W., High-Performance Fused Ring Electron Acceptor-Perovskite Hybrid. *J. Am. Chem. Soc* **2018,** *140*, 14938-14944.

(19) Jung, E. H.; Jeon, N. J.; Park, E. Y.; Moon, C. S.; Shin, T. J.; Yang, T. Y.; Noh, J. H.; Seo, J., Efficient, Stable and Scalable Perovskite Solar Cells using Poly(3-Hexylthiophene). *Nature* **2019,** *567*, 511-515.

(20) Soltani, R.; Puscher, B. M. D.; Katbab, A. A.; Levchuk, L.; Kazerouni, N.; Gasparini, N.; Camaioni, N.; Osvet, A.; Batentschuk, M.; Fink, R. H.; Guldi, D. M.; Ameribe, T., Improved Charge Carrier Dynamics in Polymer/Perovskite Nanocrystal based Hybrid Ternary Solar Cells. *Phys. Chem. Chem. Phys.* **2018,** *20*, 23674-23683.

(21) Guijarro, N.; Yao, L.; Le Formal, F.; Wells, R. A.; Liu, Y. P.; Darwich, B. P.; Navratilova, L.; Cho, H. H.; Yum, J. H.; Sivula, K., Lead Halide Perovskite Quantum Dots to Enhance the Power Conversion Efficiency of Organic Solar Cells. *Angew. Chem. Int. Ed.* **2019,** *58*, 12696-12704.

(22) Zhou, Y.; Chen, J.; Bakr, O. M.; Sun, H.-T., Metal-Doped Lead Halide Perovskites: Synthesis, Properties, and Optoelectronic Applications. *Chem. Mater.* **2018**, 30, 6589-6613.

(23) Shi, J. W.; Li, F. C.; Yuan, J. Y.; Ling, X. F.; Zhou, S. J.; Qian, Y. L.; Ma, W. L., Efficient and Stable CsPbI$_3$ Perovskite Quantum Dots Enabled by In Situ Ytterbium Doping for Photovoltaic Applications. *J. Mater. Chem. A* **2019,** *7*, 20936-20944.

(24) Kim, J.; Koo, B.; Kim, W. H.; Choi, J.; Choi, C.; Lim, S. J.; Lee, J.-S.; Kim, D.-H.; Ko, M. J.; Kim, Y., Alkali Acetate-Assisted Enhanced Electronic Coupling in

CsPbI3 Perovskite Quantum Dot Solids for Improved Photovoltaics. *Nano Energy* **2019**, 66.

(25) Abdelhady, A. L.; Saidaminov, M. I.; Murali, B.; Adinolfi, V.; Voznyy, O.; Katsiev, K.; Alarousu, E.; Comin, R.; Dursun, I.; Sinatra, L.; Sargent, E. H.; Mohammed, O. F.; Bakr, O. M., Heterovalent Dopant Incorporation for Bandgap and Type Engineering of Perovskite Crystals. *J Phys Chem Lett* **2016**, 7, 295-301.

(26) Hu, Y. Q.; Bai, F.; Liu, X. B.; Ji, Q. M.; Miao, X. L.; Qiu, T.; Zhang, S. F., Bismuth Incorporation Stabilized Alpha-$CsPbI_3$ for Fully Inorganic Perovskite Solar Cells. *ACS Energy Lett.* **2017,** *2*, 2219-2227.

(27) Protesescu, L.; Yakunin, S.; Bodnarchuk, M. I.; Krieg, F.; Caputo, R.; Hendon, C. H.; Yang, R. X.; Walsh, A.; Kovalenko, M. V., Nanocrystals of Cesium Lead Halide Perovskites ($CsPbX_3$, X = Cl, Br, and I): Novel Optoelectronic Materials Showing Bright Emission with Wide Color Gamut. *Nano Lett.* **2015,** *15*, 3692-3696.

(28) Zhu, F. P.; Yong, Z. J.; Liu, B. M.; Chen, Y. M.; Zhou, Y.; Ma, J. P.; Sun, H. T.; Fang, Y. Z., Superbroad Near-Infrared Photoluminescence from Bismuth-Doped $CsPbI_3$ Perovskite Nanocrystals. *Opt. Express* **2017,** *25*, 33283-33289.

(29) Bian, H.; Bai, D. L.; Jin, Z. W.; Wang, K.; Liang, L.; Wang, H. R.; Zhang, J. R.; Wang, Q.; Liu, S. Z., Graded Bandgap $CsPbI_{2+x}Br_{1-x}$ Perovskite Solar Cells with a Stabilized Efficiency of 14.4%. *Joule* **2018,** *2*, 1500-1510.

(30) Berends, A. C.; Donega, C. D., Ultrathin One- and Two-Dimensional Colloidal Semiconductor Nanocrystals: Pushing Quantum Confinement to the Limit. *J. Phys. Chem. Lett.* **2017,** *8*, 4077-4090.

(31) Begum, R.; Parida, M. R.; Abdelhady, A. L.; Murali, B.; Alyami, N. M.; Ahmed, G. H.; Hedhili, M. N.; Bakr, O. M.; Mohammed, O. F., Engineering Interfacial Charge Transfer in $CsPbBr_3$ Perovskite Nanocrystals by Heterovalent Doping. *J. Am. Chem. Soc* **2017,** *139*, 731-737.

(32) Zhao, Q.; Hazarika, A.; Chen, X. H.; Harvey, S. P.; Larson, B. W.; Teeter, G. R.; Liu, J.; Song, T.; Xiao, C. X.; Shaw, L.; Zhang, M. H.; Li, G. R.; Beard, M. C.; Luther, J. M., High Efficiency Perovskite Quantum Dot Solar Cells with Charge Separating Heterostructure. *Nat. Commun.* **2019,** *10*, 2842.

(33) Xiao, L. G.; He, B.; Hu, Q.; Maserati, L.; Zhao, Y.; Yang, B.; Kolaczkowski, M. A.; Anderson, C. L.; Borys, N. J.; Klivansky, L. M.; Chen, T. L.; Schwartzberg, A. M.; Russell, T. P.; Cao, Y.; Peng, X. B.; Liu, Y., Multiple Roles of a Non-fullerene Acceptor Contribute Synergistically for High-Efficiency Ternary Organic Photovoltaics. *Joule* **2018,** *2*, 2154-2166.

(34) Li, S. S.; Ye, L.; Zhao, W. C.; Zhang, S. Q.; Mukherjee, S.; Ade, H.; Hou, J. H., Energy-Level Modulation of Small-Molecule Electron Acceptors to Achieve over 12% Efficiency in Polymer Solar Cells. *Adv. Mater.* **2016,** *28*, 9423-9429.

(35) Mai, J. Q.; Lu, H. P.; Lau, T. K.; Peng, S. H.; Hsu, C. S.; Hua, W. Q.; Zhao, N.; Xiao, X. D.; Lu, X. H., High Efficiency Ternary Organic Solar Cell with Morphology-Compatible Polymers. *J. Mater. Chem. A* **2017,** *5*, 11739-11745.

(36) Mai, J. Q.; Lau, T. K.; Li, J.; Peng, S. H.; Hsu, C. S.; Jeng, U. S.; Zeng, J. R.; Zhao, N.; Xiao, X. D.; Lu, X. H., Understanding Morphology Compatibility for High-Performance Ternary Organic Solar Cells. *Chem. Mater.* **2016,** *28*, 6186-6195.

(37) Mai, J. Q.; Xiao, Y. Q.; Zhou, G. D.; Wang, J. Y.; Zhu, J. S.; Zhao, N.; Zhan, X. W.; Lu, X. H., Hidden Structure Ordering Along Backbone of Fused-Ring Electron Acceptors Enhanced by Ternary Bulk Heterojunction. *Adv. Mater.* **2018,** *30*, 1802888.

(38) Liao, H. C.; Tsao, C. S.; Lin, T. H.; Chuang, C. M.; Chen, C. Y.; Jeng, U. S.; Su, C. H.; Chen, Y. F.; Su, W. F. Quantitative Nanoorganized Structural Evolution for a High Efficiency Bulk Heterojunction Polymer Solar Cell. *J. Am. Chem. Soc*. 2011, 133, 13064−13073.

(39) Liao, H.-C.; Tsao, C.-S.; Shao, Y.-T.; Chang, S.-Y.; Huang, Y.-C.; Chuang, C.-M.; Lin, T.-H.; Chen, C.-Y.; Su, C.-J.; Jeng, U. S.; Chen, Y.-F.; Su, W.-F. Bi-Hierarchical Nanostructures Of Donor−Acceptor Copolymer And Fullerene For High Efficient Bulk Heterojunction Solar Cells. *Energy Environ. Sci*. 2013, 6, 1938−1948.

(40) Liu, C.-M.; Su, Y.-W.; Jiang, J.-M.; Chen, H.-C.; Lin, S.-W.; Su, C.-J.; Jeng, U. S.; Wei, K.-H. Complementary Solvent Additives Tune The Orientation Of Polymer Lamellae, Reduce The Sizes Of Aggregated Fullerene Domains, And Enhance The Performance Of Bulk Heterojunction Solar Cells. *J. Mater. Chem. A* 2014, 2, 20760−20769.

(41) Zhao, W. C.; Li, S. S.; Zhang, S. Q.; Liu, X. Y.; Hou, J. H., Ternary Polymer Solar Cells based on Two Acceptors and One Donor for Achieving 12.2% Efficiency. *Adv. Mater.* **2017,** *29*, 1604059.

(42) Liu, S. H.; Lin, S. H.; You, P.; Surya, C.; Lau, S. P.; Yan, F., Black Phosphorus Quantum Dots Used for Boosting Light Harvesting in Organic Photovoltaics. *Angew. Chem. Int. Ed.* **2017**, *56*, 13717-13721.

(43) Lu, L. Y.; Xu, T.; Chen, W.; Lee, J. M.; Luo, Z. Q.; Jung, I. H.; Park, H. I.; Kim, S. O.; Yu, L. P., The Role of N-Doped Multiwall Carbon Nanotubes in Achieving Highly Efficient Polymer Bulk Heterojunction Solar Cells. *Nano Lett.* **2013**, *13*, 2365-2369.